VALIDATION OF NUMERICAL MODELS FOR SEISMIC FLUID-STRUCTURE-INTERACTION ANALYSIS OF NUCLEAR, SAFETY-RELATED EQUIPMENT

Ching-Ching Yu[1], Faizan Ul Haq Mir[2], Andrew S. Whittaker[3]

[1]Ph.D. Candidate, Department of Civil, Structural, and Environmental Engineering, University at Buffalo, Buffalo, NY 14260, USA (cyu23@buffalo.edu)

[2]Ph.D. Candidate, Department of Civil, Structural, and Environmental Engineering, University at Buffalo, Buffalo, NY 14260, USA (faizanul@buffalo.edu)

[3]SUNY Distinguished Professor, Department of Civil, Structural, and Environmental Engineering, University at Buffalo, Buffalo, NY 14260, USA (awhittak@buffalo.edu)

Abstract

Seismic design, qualification, and risk assessment of nuclear safety-related vessels filled with liquid will have to consider the interaction between the vessel (tank), the contained liquid, and submerged components, if any. Seismic fluid-structure-interaction (FSI) analysis of nuclear vessels will rely on numerical models, which are required to be verified and validated. This study validates previously-verified numerical models using test data generated from earthquake-simulator experiments involving a cylindrical tank. Two solvers in LS-DYNA for FSI simulations are used for the numerical analysis: Arbitrary-Lagrangian-Eulerian (ALE) and Incompressible Computational Fluid Dynamics (ICFD). Numerical and test results are compared for responses critical to seismic design of advanced reactor vessels: hydrodynamic pressures on the tank wall, reactions at the support, and wave heights of the contained liquid. Analysis is performed for one-, two-, and three-directional seismic inputs with a range of intensity, and rocking motions. The accuracy of the numerical results and different methods for outputting wave heights are discussed. Recommendations for validation of seismic FSI numerical models of advanced reactors are provided. The validation exercise presented in this study is broadly applicable to cylindrical tanks, regardless of industry sector.

Keywords: seismic fluid-structure interaction, validation of numerical models, ALE, ICFD, ARPA-E

1. Introduction

A liquid-filled advanced nuclear reactor includes a vessel and components submerged in a liquid coolant. Figure 1 (Gluekler, 1997) presents a prototype sodium fast reactor, which is composed of a vessel filled with liquid sodium and housing internal components. Different from the pressurized water reactors (PWRs) and boiling water reactors (BWRs) in the US nuclear fleet, which are pressurized to increase the boiling point of the fluid, these advanced reactors operate at low pressure but relatively high temperature to maintain the coolant (e.g., liquid metal or molten salt) in the liquid phase. Because these advanced reactors operate at low overpressures, the vessel wall thickness is much less than that in either a PWR or a

BWR. However, the substantial reduction in wall thickness is accompanied by a significant increase in seismic vulnerability, and so the effects of earthquake shaking, which induces fluid-structure interaction (FSI) in/on the vessel, must be considered in the design, qualification, and risk assessment.

Seismic FSI analysis for the design of first and second generation nuclear reactors used closed-form (analytical) solutions (Thomas et al., 1963) because there were no suitable computational tools. The seismic FSI analysis was parsed into: 1) interaction of the vessel (tank) and the contained liquid, and 2) interaction of the internal components and the surrounding liquid. Analytical solutions for seismic FSI of tanks were first developed by Jacobsen and his co-workers at Stanford University (e.g., Hoskins and Jacobsen, 1934; Jacobsen, 1949) and were subsequently extended and/or modified to accommodate different boundary conditions and seismic inputs (e.g., Veletsos and Tang, 1986, 1987; Bandyopadhyay et al., 1995; Yu and Whittaker, 2020a; Mir et al., 2021). Veletsos (1984) and Yu and Whittaker (2020b) review prior work. Analytical studies for seismic FSI analysis of submerged components for application to nuclear reactors were led by the Argonne National Laboratory (ANL) in the 1970s (Chen and Rosenberg, 1975; Chen et al., 1976; Chung and Chen, 1976, 1977). Dong (1978) summarized studies on submerged components, including those at ANL. These analytical studies on tanks and submerged components assumed standard geometries (e.g., a cylinder or a rectangle) and boundary conditions (e.g., fixed or pinned), linear-elastic response, and idealized inputs (e.g., small-amplitude unidirectional inputs). No available analytical solutions accommodate the geometries and boundary conditions of reactors and multi-directional seismic inputs. If an advanced reactor vessel is subjected to strong earthquake shaking, liquid (fluid) responses could be nonlinear, including sloshing and disengagement from the inner surfaces of the vessel and submerged components, none of which can be calculated analytically.

In the modern era, seismic FSI analysis of advanced nuclear reactors will rely on numerical simulations to compute *linear* and *nonlinear* fluid responses. Herein, linear and nonlinear are defined on the basis of geometry at the free surface of the contained liquid. If displacements are small (e.g., no wave action or sloshing), the response is deemed *linear*. If displacements are large (e.g., wave action and/or disengagement of the fluid from the wall of the vessel), the response is deemed *nonlinear*. Numerical models calculate nonlinear fluid responses using fluid-mechanics solvers, including adaptive meshing routines or defining fluid in a control volume (fluid domain) without discretization. Structural mechanics solvers compatible with fluid elements and/or fluid materials can be used to calculate linear responses, but a challenge with such analysis is justifying the assumption of linear fluid response, which will depend on the intensity and frequency content of the seismic input, the dimensions of the vessel, the freeboard for the contained liquid, and the presence of components inside the vessel. Table 1 introduces fluid-mechanics solvers for nonlinear analysis and fluid elements and materials for linear analysis implemented in computer codes: ANSYS (ANSYS Inc., 2005), ABAQUS (Dassault Systèmes, 2018), LS-DYNA (LSTC, 2018a), OpenFOAM (OpenCFD Ltd., 2020), and OpenSees (Mazzoni et al., 2009). The listed solvers, elements, and materials are capable of calculating fluid responses, but some of them are not suitable for seismic FSI analysis of liquid-filled tanks. (For example, the fluid material MAT_ACOUSTIC in LS-DYNA listed in Table 1 cannot calculate seismic hydrodynamic responses (Huang, 2020).) The capability of a solver, element, or material must be explored before use for seismic FSI analysis, regardless of whether the fluid responses are linear or nonlinear.

Before being used for seismic design, equipment qualification, or risk assessment in nuclear facilities, numerical models should first be verified and validated. Numerical models can be verified by comparing results with those calculated using analytical solutions. A verified numerical model can then be validated using data from large-scale physical testing. This paper demonstrates a process of validation for numerical models for seismic FSI analysis of liquid-filled vessels (tanks) by comparing numerical and experimental results. (Verification of numerical models for FSI analysis of tanks can be found in Goudarzi and Sabbagh-Yazdi (2012) and Yu and Whittaker (2020c)).

A number of studies have addressed validation of FSI models, but none, to the knowledge of the authors, have considered all fluid-structure responses critical to seismic design of reactor vessels (e.g., pressures, reactions at supports, and wave heights) for three-directional earthquake shaking. Myrillas et al. (2017) qualitatively compared numerical simulations and test images of nonlinear waves in a cylindrical tank, driven by unidirectional, horizontal, sinusoidal motions. Radnić et al. (2018) compared numerical and test data for pressures on a wall of a rectangular tank, and Compagnoni and Curadelli (2018) compared those for wave heights in a cylindrical tank. The inputs used in the studies (Radnić et al.; Compagnoni and Curadelli) were unidirectional and horizontal, with an amplitude less than 0.5 g. Validation studies for liquid-filled reactors including internal components are available, but limited seismic responses were reported. Examples are Fujita et al. (1984) and Park et al. (2014), which compared numerical and test data for modal frequencies of and/or wave heights in reactor models with a length scale of 1/10 to 1/4.

Validation of numerical models for FSI analysis in support of seismic design, qualification, and risk assessment of advanced reactor requires a robust dataset and the supporting metadata. Although numerous experimental studies have focused on the seismic responses of tanks (e.g., Hoskins and Jacobsen, 1934; Morris, 1938; Haroun, 1983; Chalhoub and Kelly, 1988; Calugaru and Mahin, 2009; Pal et al., 2001; Sangsari and Hosseinzadeh, 2014), none provide sufficient and usable information (e.g., pressures, reactions at supports, wave heights, and metadata) to validate models for intense, three-directional earthquake shaking.

To enable validation, fluid-structure responses of a base-supported cylindrical tank were generated using a six-degree-of-freedom earthquake simulator at the University at Buffalo. The dimensions of the tank were selected based on the capacity of the earthquake simulator and a ratio of height-to-radius that is common to some prototype advanced reactors. The test tank had a simple geometry, internal components were excluded for the studies described herein, and the material (i.e., carbon steel), contained liquid (i.e., water), and supporting condition (at the base) were different from those of many reactor vessels: see Figure 1. Test data were/are in part used in Mir et al. (2020a) and this paper with different foci. Mir et al. (2020a) investigated 1) the need for nonlinear numerical models for seismic FSI analysis of tanks, 2) damping ratios associated with wave actions, and 3) the impacts of seismic (base) isolation on fluid-structure responses of tanks. This paper 1) validates previously-verified, nonlinear, FSI models for intense shaking, 2) identifies limitations and challenges in experimental measurements and numerical analysis, and 3) presents recommendations for validating a numerical model for seismic FSI analysis of safety-related nuclear vessels and structures.

Mir et al. (2020a) compared measured fluid-structure responses of the test tank with those calculated using linear and nonlinear numerical models and analytical solutions. The study considered multi-directional seismic motions with peak ground accelerations (PGAs) less than 0.5 g. Numerical calculations were performed using LS-DYNA: the material MAT_FLUID_ELASTIC for the fluid in linear analysis and the Arbitrary Lagrangian-Eulerian (ALE) solver for nonlinear analysis. Analytical solutions (e.g., Veletsos, 1984) developed for unidirectional seismic motion were used to estimate fluid-structure responses. Responses for multi-directional input were assumed to be algebraic sums of those analytically calculated for one-component motions in different directions. Mir et al. (2020a) calculated damping ratios for wave actions using the attenuation of wave heights with the passage of time, and investigated the effects of seismic isolation on responses of the test tank and the contained fluid.

This paper performs a validation study of nonlinear numerical models by comparing results with data from experiments for the tank as described in Mir et al. (2020a), but using inputs with greater amplitudes: PGA=0.1 to 1 g. The models used here were previously verified in Yu and Whittaker (2020c) using analytical solutions (Veletsos, 1984; Jacobsen, 1949; Yu and Whittaker, 2020b). Data from earthquake-simulator tests for the tank equipped with central and off-center internal components (Mir et al. 2020b; 2020c) will be used for validation of verified models (Yu and Whittaker, 2021) and reported elsewhere. These verified and validated models for tanks and submerged components will, together, enable seismic FSI analysis of advanced nuclear reactors.

The seismic FSI analysis here is performed per two fluid-mechanics solvers in LS-DYNA: ALE, which was used in Mir et al. (2020a), and Incompressible Computational Fluid Dynamics (ICFD). The numerical and test results are compared for hydrodynamic pressures on the tank wall, shear forces and moments at the tank base, and wave heights. Accuracy and limitations of experimental measurements, nonlinear numerical analysis, and methods used for outputting wave heights, which involve tracking the displacement of the free surface, are described.

Section 2 presents the earthquake-simulator tests, including the test tank, instrumentation, and input motions. Section 3 describes the ALE and ICFD models of the test tank. Section 4 presents input motions used in the numerical models, generated using the acceleration at the tank base measured in the tests. Section 5 validates the models of Section 3 by comparing the numerical and test results of fluid-structure responses. Section 6 provides recommendations for validating a numerical model for seismic FSI analysis of safety-related nuclear vessels, and presents a summary and conclusions of the validation exercise.

The software package LS-DYNA is used exclusively for the studies described in this paper. This package is one of a number of codes used by industry for seismic FSI analysis, as noted previously. The key cards used to build the numerical models are identified below to enable a reader to either replicate the models in LS-DYNA or help build a model in another commercial finite element code.

2. Earthquake-simulator tests for a base-supported tank

A base-supported, cylindrical, steel tank was tested using a six-degree-of-freedom earthquake simulator at the University at Buffalo. Figures 2a and b present the tank and the simulator, respectively, together with coordinates (*x*, *y*, *z*) and cardinal directions (*N*, *S*, *E*, *W*) in the panel b. The tank was constructed with a carbon steel pipe and a base plate, and filled with water. The height of the pipe, H_s, is 2 m and the radius, R, is 0.76 m: the ratio of height-to-radius, $H_s / R = 2.5$, is common to some prototype advanced reactors. The thickness of the pipe (tank wall), h, is 7.92 mm. A 76.2 mm-wide, 25.4 mm-thick flange is welded to the top of the tank. The height of the contained water, H, is 1.6 m. The overall dimensions of the tank were based on the capacity of the earthquake simulator and the plan to subject the model to intense, three-directional earthquake shaking. The first impulsive frequency (i.e., $f_{imp,1}$, lateral frequency) of the water-filled tank is 140 Hz and the first convective frequency (i.e., $f_{con,1}$, frequency of wave action) is 0.77 Hz, both estimated using analytical solutions (Veletsos, 1984).

The instrumentation for the experiments is presented in Figure 3, including pressure transducers, load cells, Temposonic gauges, and accelerometers, together with the global coordinate system (*x*, *y*, *z*). Figure 3a presents the names of the pressure transducers, which are arranged at three different heights and in arrays of four: +*x* (east), -*x* (west), +*y* (north), and -*y* (south) faces of the tank wall. Figure 3b presents the four load cells, denoted *LNE*, *LNW*, *LSE* and *LSW*, identifying their locations at the north-east, north-west, south-east, and south-west corners of the base plate, respectively. Each load cell is capable of measuring axial force, shear forces in two horizontal directions, and moments about two horizontal axes at its center (i.e., mid-height). Figure 3c presents two Temposonic gauges, *TE* and *TW*, used to measure wave heights at distances of 51 mm (2.5") from the +*x* (east) and -*x* (west) faces of the tank wall. The wave-height transducer was designed per Mir et al. (2019). In Figure 3c, a float is attached to a lightweight tube that is mounted onto the waveguide of a Temposonic gauge. A magnet is attached to the top of the tube. The Temposonic gauge records the vertical motion of the magnet, which is driven by the movement of the float. Figure 3d presents the names of the accelerometers on the base plate, located near its four corners and at its center. Each accelerometer measures motions in one direction. Three accelerometers are used at each location shown as a triangle to measure three-directional motions. The solid circle at the center of the base plate indicates the use of one accelerometer to measure the motion in the *z* direction. Data from other instrumentation, including strain gauges and accelerometers on the tank wall and cameras supporting image processing for wave actions, are not used in this paper and so are not introduced here. Details can be found in Mir et al. (2019; 2020b; 2020c).

The earthquake-simulator tests involved 100+ sets of input motions. The input motions included white noise, sine waves, and one-, two-, and three-directional earthquake shaking extracted from ground motion records. Responses generated by three motions are used here for validation: ES-1, ES-2, and ES-3, where ES denotes earthquake-simulator (ES) input. Table 2 presents information on the three inputs. The three motions are five-second acceleration time series, extracted from the earthquake records noted in Table 2, after time compression (see the eighth column in Table 2), but including their strong motion. The peak ground accelerations (PGAs) of the *x* components of ES-1, ES-2, and ES-3 are scaled to 1 g, 0.1 g, and 0.1 g, respectively. The *y* component of ES-2 and the *y* and *z* components of ES-3 are scaled using the corresponding scale factors for their *x* components. The scaling enables ES-1 to represent a strong motion, and reduces the intensity of ES-2 and ES-3 to prevent the outflow of the contained water due to sloshing. Figure 4 presents the time series of ES-3, including *x*, *y*, and *z* components. Figure 5 presents the response spectra of the three ES inputs, for 2% damping. The three inputs have very different frequency contents with overlapping ranges, which provides wide and challenging dynamic characteristics in responses for the validation study.

3. Numerical models

Numerical analysis is performed using the ALE and ICFD solvers in LS-DYNA (2018b, 2019)[1], both of

[1] Different versions of LS-DYNA are used here: SMP_d_Dev_126632 (2018b) is used for the ALE analysis and SMP_d_R11_1 (2019) is used for the ICFD analysis.

which are capable of predicting nonlinear fluid responses. The ALE solver uses an explicit analysis and models fluid using Eulerian elements. These elements do not deform but rather serve together as a grid in the fluid domain. The fluid can flow through grid cells (i.e., Eulerian elements), in which integration points for calculating fluid responses are located. The ICFD solver adopts an implicit analysis to model a fluid using Lagrangian elements. These elements are highly deformable. An adaptive meshing routine can be implemented (but is not used here): if the fluid elements deform to a defined tolerance, a number of smaller elements are automatically generated to accommodate large deformations of the fluid.

Numerical models for the ALE and ICFD solvers are constructed for the test tank shown in Figure 2a: $H_s = 2$ m, $R = 0.76$ m, $h = 7.92$ mm, and $H = 1.6$ m. The flange at the top of the tank and the four load cells, which support the tank on the earthquake simulator, are not included in the models.

Figure 6 presents the ALE model and global coordinates (*x*, *y*, *z*). Figure 6a shows the elements of the tank wall (blue) and the base plate (red). Figure 6b shows the elements of the fluid domain: water (yellow) topped by a vacuum space (grey). Air is not included in the model. The sizes of the elements shown in Figures 6a and b are optimized, resulting in smaller fluid elements adjacent to the tank wall and around the boundary between the water and the vacuum (i.e., free surface). The tank wall and the base plate are modeled using 3360 and 2748 Lagrangian, four-node, shell elements, respectively. The water and the vacuum are modeled using 63360 and 17280 Eulerian, eight-node, solid elements, respectively. The tank and the fluid domain (including the water and vacuum) share nodes at their interfaces. Figure 6c presents the water in the tank at the first step of the analysis (i.e., time t=0).

Tracers (black dots in Figure 6c) that track the motion of the free surface are assigned using the *DATABASE_TRACER card to output wave heights (Do, 2019). These tracers move with the velocities of the fluid in the three directions, and their *z* coordinates are used to calculate wave heights. There are one hundred twenty-four tracers located on and near the free surface, along the *x* direction, and near the $\pm x$ faces of the tank wall. Sixty-two tracers are placed near each face and in two layers (i.e., 31 tracers in each layer), as shown in the magnified view in Figure 6c. The two layers are located on and 10 mm below the free surface. The tracers span $x = R$ (0.76 m) to 0.62 m and -0.62 m to -0.76 m, and cover the measuring locations of the Temposonic gauges *TE* and *TW*, which are 51 mm away from the $\pm x$ faces of the wall (see Figure 3c). The tracers on the free surface (upper layer) are used to output wave heights.

Figure 7 presents the ICFD model and global coordinates (*x*, *y*, *z*). Figure 7a shows the elements of the tank wall (blue) and the base plate (red). Figure 7b presents one half of the fluid domain, which is defined using three surfaces: 1) adjacent to the tank base (pink), 2) adjacent to the tank wall (yellow), and 3) horizontally closing the top of the domain (grey). The height of the fluid domain is 1.8 m, providing a sufficient freeboard of 0.2 m ($H = 1.6$ m) to prevent overtopping by waves. (The vertical displacement of the free surface in the tank is less than 0.2 m; see Section 5.3 and Figure 17.) As presented in Figure 7b, a finer fluid mesh is used along the *x* and *y* directions across the diameter of the grey surface and in the top 0.4 m of the yellow surface, where wave actions are expected to be relatively significant. The tank wall and the base plate are modeled using 7820 and 2700 Lagrangian, four-node, shell elements, respectively. The fluid surfaces are modeled using 13840 Lagrangian, three/four-node, shell elements. The tank and the fluid surfaces do not share nodes at their interfaces. Their interaction is activated by the *ICFD_BOUNDARY_FSI card.

Lagrangian, four-node, solid elements for the fluid enclosed by the three surfaces in Figure 7b are automatically generated by the ICFD solver at t=0: Figure 7c. The initial height of the free surface, H = 1.6 m, is defined using the *ICFD_INITIAL_LEVELSET card. The *MESH_BL and *MESH_SIZE_SHAPE cards are used to generate finer elements adjacent to the tank wall and around the free surface, respectively, as shown in the *x-z* cross section of the fluid domain of Figure 7d. A finer mesh around the free surface results in more accurate simulation for wave actions.

Two methods are used for outputting wave heights in the ICFD analysis: 1) *ICFD_DATABASE_POINTOUT card, and 2) ***Floater*** option in the graphical user interface (GUI) of LS-Prepost (2018c)[2] (Caldichoury, 2019). In the first method, tracers that move with the fluid velocity, similar to those used in the ALE model, are assigned on the free surface per the *ICFD_DATABASE_POINTOUT card. Fifty-eight tracers span $x = R$ (0.76 m) to 0.62 m and -0.62 m to -0.76 m, with a spacing of 5 mm: covering the measuring locations of the Temposonic gauges ***TE*** and ***TW***. At each tracer, its *z* coordinate and depth (i.e., vertical distance between the free surface and the tracer; termed ***levelset*** in LS-DYNA) are recorded. The sum of the *z* coordinate and depth time series is used to calculate wave heights. The tracers used for the ICFD analysis are not visualizable in the GUI and so are not shown in Figure 7. In the second method, ***Floaters*** are fixed at the assigned *x* and *y* coordinates and float on the free surface. Their *z* coordinate time series (termed ***height*** in the GUI) are used to calculate wave heights. The floaters are horizontally stationary (*x* and *y* directions), but the tank moves with seismic input in the three directions. To enable recording the *z* coordinates of the free surface around ***TE*** and ***TW***, the floaters span *x*=0.65 m to 0.77 m and *x*=-0.77 m to -0.65 m with a spacing of 5 mm, to accommodate the displacement of the tank in the *x* direction (≤ 50 mm).

[2] Floater data are saved in a state database (termed *d3plot* file in LS-DYNA) and output through the GUI of LS-Prepost. The d3plot file includes animations at assigned time steps. To generate wave height time series using floater data, a small time interval (e.g., $\Delta t = 0.05$ second) is required for the d3plot file.

The elements of the tank wall and the base plate are assigned elastic and rigid materials, respectively, with mechanical properties consistent with carbon steel, including a density ρ_s of 7880 kg/m^3, an elastic modulus E_s of 2×10^{11} N/m^2, and Poisson's ratio υ_s of 0.27. (The values of E_s and υ_s do not affect the responses of the rigid base but must be included in the rigid material definition in the LS-DYNA.) A damping ratio of 2% (Malhotra et al., 2000; CEN 1998) is assigned to the elements of the wall for a frequency range of 20 to 300 Hz using the *DAMPING_FREQUENCY_RANGE_DEFORM card (Huang et al., 2019). Note that numerical results of the tank here are not affected by the damping ratio because $f_{imp,1} = 140$ Hz and significant spectral accelerations of the inputs are at frequencies less than 80 Hz, as shown in Figure 5.

The mechanical properties consistent with water at 25°C are used for the elements of the water in the numerical models. A density ρ_w of 1000 kg/m^3, a dynamic viscosity μ_w of 10^{-3} N/m^2-s, and a bulk modulus, K_w, of 2.15×10^9 N/m^2 are assigned to the water elements in the ALE model (shown as yellow in Figure 6b). Identical values of ρ_w and μ_w are used for the elements of the fluid surfaces adjacent to the tank wall and base in the ICFD model (shown as yellow and pink in Figure 7b), but the bulk modulus is not used because the solver can accommodate only an incompressible fluid. The elements of the vacuum space in the ALE model, shown in grey in Figure 6b, are assigned void properties through the *INITIAL_VOID card. The elements of the top surface of the fluid domain in the ICFD model, shown as grey in Figure 7b, are assigned the ***vacuum properties*** with zero density and viscosity (i.e., $\rho_v = 0$ and $\mu_v = 0$), and the ***vacuum option*** (*FLG*=0) in the *ICFD_MAT card is activated.

The mechanical properties assigned to the elements of the tank, water, and vacuum are listed in Table 3. The masses of the numerical models are listed in Table 4, and the total mass is 4929 kg. The gravitational acceleration g of 9.81 m/s^2 is assigned to the ***z*** direction.

4. Input motions for numerical models

Accelerations of the base plate measured in the experiments are used as input motions for the response-history analysis of the numerical models. As shown in Figure 3d, twelve accelerometers are placed around the four corners of the base plate: *ANE1X* (*Y*, *Z*), *ANW1X* (*Y*, *Z*), *ASE1X* (*Y*, *Z*), and *ASW1X* (*Y*, *Z*). Each triangle in the figure indicates three accelerometers that measure respective motions in the ***x***, ***y***, and ***z*** directions, based on the coordinates shown in Figure 2b. Earthquake-simulator (ES) inputs used for the experiments are not directly used for the numerical models because the four load cells supporting the test tank on the simulator are neither rigid nor included in the models. The four load cells introduced flexibility at the tank support in the experiments, and rocking motions were observed for horizontal excitations. An ES input in the *x* (*y*) direction generates a translational motion in the *x* (*y*) direction and a rocking motion about the *y* (*x*) axis on the base plate. An ES input in the *z* direction generates a translational motion in the *z* direction and out-of-plane (vertical) deformation of the base plate. The base plate is assumed to be rigid in the numerical models, and the vertical deformation is not included in the analysis. To enable comparisons of numerical and test results, the measured responses associated with the frequency of the out-of-plane deformation of 37 Hz[3] are removed. A band-stop filter designed for 32 to 42 Hz is used to process the base plate acceleration data. A MATLAB script, OpenSeismoMatlab (Papazafeiropoulos and Plevris, 2018), is used to correct the baseline of the accelerations of the base plate generated in the tests to avoid unrealistic and significant displacements due to measuring errors. The translational and rocking motions are derived using the filtered and baseline corrected accelerations, and are used as input time series at the center of the rigid base plate in the numerical models.

The translational input motions, acc_x, acc_y, and acc_z, for the numerical models are derived using the average accelerations measured around the four corners of the base plate in a given direction. Figure 8 presents the calculations of the rocking input motions, acc_{rx} and acc_{ry}, for the numerical models. The black square in each panel is the plan view of the base plate. The black solid circles are accelerometers located near the four corners of the plate, *ANE1Z*, *ANW1Z*, *ASE1Z*, and *ASW1Z*, and the red arrows and text represent measured accelerations in the *z* direction. The blue arrows and text represent the rocking accelerations, acc_{rx} and acc_{ry}, used as inputs for the numerical models, derived using the measured accelerations. Assuming that the base plate is rigid, per Figure 8a, acc_{rx} is calculated as the sum of the ***relative*** vertical accelerations on the north face (*ANE1Z*, *ANW1Z*), with respect to those on the south face (*ASE1Z*, *ASW1Z*), divided by $2\,d_y$, where d_y is the distance between the accelerometers in the *y* direction (1280 mm). Similarly, per Figure 8b, acc_{ry} is calculated using the sum of the relative vertical accelerations on the west face (*ANW1Z*, *ASW1Z*), with respect to those on the east face (*ANE1Z*, *ASE1Z*), by $2\,d_x$, where d_x is the distance between the accelerometers in the *x* direction (1220 mm).

Multi-directional time series, NM-1, NM-2, and NM-3, for the numerical analysis are derived using measured accelerations of the base plate for ES-1, E-2, and ES-3, respectively. (The "NM" denotes numerical-model inputs whereas "ES" denotes earthquake-simulator inputs.) Table 5 presents information for NM-1, NM-2, NM-3. Figure 9 presents the time series of NM-3, including the three translational

---

[3] The empty tank was tested using white noise in the vertical direction, and the vertical motion at the center of the base plate was measured using *AC1Z* shown in Figure 3d. The Fourier amplitude spectrum of the motion shows a peak at 58 Hz, which is the frequency of the out-of-plane motion of the base plate, f_{out}, for the empty tank. Considering that f_{out} is proportional to $1/\sqrt{m}$ ($m = 2011$ kg, if empty, and 4929 kg, if $H = 1.6$ m; see Table 4), the value of f_{out} for the tank with a water depth of 1.6 m is expected to be 37 Hz.

components, *x*, *y*, *z*, and two rocking components, *rx*, *ry*. Figure 10 presents acceleration response spectra for the three NM inputs, calculated using a damping of 2% of critical.

5. Results and validation

Fluid-structure responses calculated using the ALE and ICFD models for inputs NM-1, NM-2, and NM-3 are compared with those measured in the earthquake-simulator tests for ES-1, ES-2, and ES-3, respectively. The reported responses include hydrodynamic pressures on the tank wall, reactions at the center of the tank base, and wave heights of the contained water. (Numerical and experimental data for these responses involve both impulsive and convective components; see Yu and Whittaker (2020b) for details.) Since the base plate is rigid in the models, a band-stop filter designed for 32 to 42 Hz is used for the test data to remove motion associated with the out-of-plane deformation of the plate (see footnote 3) to enable the comparison. As presented in Section 4, the NM inputs are accelerations at the base plate generated by the ES inputs: the base plate motions in the numerical models and the test specimen are essentially identical. Accordingly, NM and ES inputs are not distinguished hereafter and are both characterized using NM-1, NM-2, and NM-3.

The numerical analysis for each input motion is performed for 6 to 7 seconds. The run times of the ALE and ICFD analyses are around 27 hours and 8 days[4], respectively, on a computer with 7th Gen (i7) 4-core Intel processor, 32 GB RAM, and 512 GB SSD.

5.1. Hydrodynamic pressure

The hydrodynamic pressures on the tank wall, p_w, measured by the twelve pressure transducers *PN1* (*2*, *3*), *PS1* (*2*, *3*), *PE1* (*2*, *3*), and *PW1* (*2*, *3*) shown in Figure 3a are compared with those calculated using the numerical models. Figure 11 enables a comparison of the ALE and test results for the pressures on the west face of the tank wall, $p_{w,W}$, and Figure 12 presents companion data for the ICFD model. Time series for the pressures on the north, south, and east faces of the tank wall (i.e., $p_{w,N}$, $p_{w,S}$, and $p_{w,E}$) can be found in Yu and Whittaker (2020c).

5.2. Reactions: shear forces and moments at the tank base

The reactions at the center of the tank base, including translational forces in the *x*, *y*, and *z* directions (i.e., F_x, F_y, and F_z) and moments with respect to the *x* and *y* axes (i.e., M_x and M_y), calculated using the

[4] If the tank is considered to be rigid, namely no deformations, the model can exclude the tank and include the fluid domain (i.e., water and vacuum) only. The run times of the ALE and ICFD analyses for this model are 13 and 21 hours, respectively. The analysis calculates fluid responses, including wave heights and hydrodynamic pressures on the domain boundaries (adjacent to the tank wall and base), and these results can be compared with test data. However, since the tank is not present in this alternate model, reactions at the support exclude the contribution of its inertial force and are not comparable with test data.

numerical models and measured in the tests are compared in Figures 13 and 14. Test results for these reactions are derived using output data from the four load cells, *LNE*, *LNW*, *LSE* and *LSW*, shown in Figure 3b. The data output by each load cell include two shear forces, $F_{L_i,x}$ and $F_{L_i,y}$, an axial force, $F_{L_i,z}$, and two moments, $M_{L_i,x}$ and $M_{L_i,y}$, where $i=1$ to 4 and $L_1 = LNE$, $L_2 = LNW$, $L_3 = LSE$, and $L_4 = LSW$. These forces and moments are output with respect to the center (mid-height) of each load cell. The reaction forces F_x, F_y, and F_z at the center of the tank base are the summations of the load-cell data in the given directions, $\sum_{i=1}^{4} F_{L_i,x}$, $\sum_{i=1}^{4} F_{L_i,y}$, and $\sum_{i=1}^{4} F_{L_i,z}$, respectively. The reaction moments, M_x and M_y, at the center of the tank base are derived using load-cell data as indicated in Figure 15. Figure 15a is a plan view of the base plate, the four load cells, and the reaction moments, M_x and M_y (shown in blue), together with coordinates (*x*, *y*, *z*) and cardinal directions (*N*, *S*, *E*, *W*). Figures 15b and c present the *N-S* and *E-W* sections, respectively, and the load-cell forces, $F_{L_i,x}$, $F_{L_i,y}$, $F_{L_i,z}$, $M_{L_i,x}$, and $M_{L_i,y}$. On the *N-S* section of Figure 15b, M_x is calculated as:

$$M_x = \sum_{i=1}^{4} M_{L_i,x} + \sum_{i=1}^{4} F_{L_i,y} \cdot (h_z / 2) + (F_{LNE,z} + F_{LNW,z} - F_{LSE,z} - F_{LSW,z}) \cdot (d_y / 2) \tag{1}$$

where d_y is the distance between the centers of two load cells in the *y* direction (916 mm; shown in green), and h_z is the height of the load cells (350 mm; shown in orange). Similarly, on the *E-W* section of Figure 15c, M_y is calculated as:

$$M_y = \sum_{i=1}^{4} M_{L_i,y} - \sum_{i=1}^{4} F_{L_i,x} \cdot (h_z / 2) + (F_{LNW,z} + F_{LSW,z} - F_{LNE,z} - F_{LSE,z}) \cdot (d_x / 2) \tag{2}$$

where d_x is the distance between the centers of two load cells in the *x* direction (916 mm; shown in green). Figure 13 enables a comparison of ALE and test results for F_x and M_y, and Figure 14 presents companion data for the ICFD model. The time series for F_y, F_z, and M_x can be found in Yu and Whittaker (2020c).

5.3. Wave height

Wave heights (with respect to the initial level of the free surface), $d_{w,E}$ and $d_{w,W}$, measured by the Temposonic gauges *TE* and *TW* shown in Figure 3c, respectively, are compared with those calculated using the numerical models in Figures 16 and 17. The wave height in the models at a monitoring location (*TE* or *TW*) at each time step is calculated by interpolating the output data of its two adjacent tracking points on the free surface (i.e., tracers in the ALE model; tracers and floaters in the ICFD model). Figure

16 enables a comparison between ALE and test results. The ALE results are calculated using the *z* coordinates of the tracers on the free surface shown in Figure 6c. Figure 17 presents companion results for the ICFD model. The ICFD results are calculated using two datasets, as described in Section 3: 1) the sum of the *z* coordinate and levelset of the tracers, and 2) the *z* coordinate of the floaters.

5.4. Discussion

Table 6 presents the maximum absolute values (amplitudes) of hydrodynamic pressures on the tank wall, p_w; reactions at the center of the tank base, F_x, F_y, F_z, M_x, and M_y; and wave heights, d_w. The values are extracted from the time series of the test, ALE, and ICFD data for NM-1, NM-2, and NM-3. Since NM-1 does not include *y* and *z* components, the pressures on the $\pm y$ faces of the tank wall, $p_{w,N}$ and $p_{w,S}$, and reactions, F_y, F_z, and M_x, are tiny and not reported. Similarly, NM-2 does not include a *z* component, and so F_z is not reported. The percentage differences between the ALE (and ICFD) and test results are presented in parentheses in Table 6. Differences greater than $\pm$10% are bolded. If the differences in a response are less than or equal to $\pm$10% for all three seismic inputs, the model is considered herein to be validated for calculating the response. (The threshold for validation is problem- and analyst-specific, and could be considered too lenient for base reactions and too stringent for wave heights.)

As seen in Figures 11 and 12, the numerical (ALE and ICFD) and measured time series of hydrodynamic pressure $p_{w,W}$ are in excellent agreement at ***PW1*** and ***PW2***, but differences in the amplitude are evident at ***PW3***. Per Table 6, the differences between the ALE and test results for $p_{w,E}$, $p_{w,W}$, $p_{w,N}$, and $p_{w,S}$ are generally less than $\pm$10%, except for those at ***PW3*** for NM-2 and at ***PN3*** for NM-3: -23% and -14%, respectively. Similarly, the differences between the ICFD and test results are also typically less than or equal to $\pm$10% except for ***PE3*** and ***PW3*** for NM-1, ***PW3*** for NM-2, and ***PN3*** for NM-3: -14% to 18%. These 10+% differences between the numerical and test results are all at a height of 1524 mm above the tank base (see ***PE3***, ***PW3***, and ***PN3*** in Figure 3a) and close to the free surface of the contained water ($H = 1.6$ m). Hydrodynamic pressures around the free surface are significantly affected by wave actions, for which calculations are challenged using the ALE and ICFD solvers. (The inability to predict wave heights is described later in this section (5.4).)

As shown in Figures 13 and 14, the numerical and test results for F_x and M_y at the center of the tank base for each motion agree well. Per Table 6, the differences between the ALE (and ICFD) and test results for the amplitudes of F_x, F_y, F_z, M_x, and M_y are all less than or equal to $\pm$10%, for the three seismic inputs.

As seen in Figures 16 and 17, the ALE and ICFD time series of wave heights are in-phase with the measured responses, but differences in their amplitudes warrant further investigation. Per Table 6, the differences in the maximum wave heights between the test and ALE results, which are output using the tracers, range between -9% and 58%, and those for the ICFD data range between -9% and 34%, output using the tracers, and between -15% and 42%, output using the floaters.

The most significant differences for wave heights are at TE for NM-1 (see $d_{w,E}$ in Table 6a): 58% for the ALE model, and 34% and 42% for the ICFD model. These differences are attributed to errors in numerical (ALE and ICFD) analysis and chaotic fluid responses on the free surface seen in the experiment. The numerical errors are associated with the efficacy of wave simulation and the methods for outputting wave-height data. The ALE solver does not simulate waves accurately in part due to the boundary effect (Do, 2019): the vertical fluid velocity adjacent to the tank wall is zero and waves near the wall do not form correctly. Per Yu and Whittaker (2020c), the wave height is zero at $x = R$ and fluctuates in $\pm 0.9 \le x / R \le \pm 1$, in an ALE model similar to that used here. (More details on the boundary effect are presented in Section 4 of Yu and Whittaker (2020c).) Per Figure 3c, the Temposonic gauge TE is located 51 mm from the east face of the tank wall, at $x / R = 0.93$ ($R = 762$ mm, x= R-51 mm=711 mm), where wave height in the ALE model is not calculated accurately. In terms of the method used for outputting wave heights, the tracers do not necessarily float on the free surface. Figure 18a presents the tank, contained fluid (shown in blue), and tracers (black dots) in the ALE model for NM-1 at the time of the maximum $d_{w,E}$: 1.5 seconds per Figure 16a. A portion of the free surface and tracers around the monitoring location of TE are magnified in the figure. The x coordinate of the monitoring location and five z coordinates are denoted: x=711 mm and z=1600 (original free surface, $H = 1.6$ m), 1700, 1725, 1749, and 1750 mm. As shown in Figure 18a, for $x \ge 711$ mm, the tracers in the two layers converge. At x=711 mm, the free surface (top of the blue part) is at z=1725 mm, whereas the level of the tracer that is identified with a green line is at z=1749 mm. Based on the tracer data at 1.5 seconds, the maximum $d_{w,E}$ of the ALE model is 149 mm ($d_{w,E}$ =z- H =1749-1600=149 mm; see Table 6a). Although the tracer should float on the free surface, it does not, and lies above the surface by 24 mm (1749-1725=24) at 1.5 seconds, which contributes to an overestimation of 26%, by comparison with the test results of 94 mm per Table 6a (i.e., 24/94=26%). For the ICFD analysis, the free surface is defined through the *ICFD_INITIAL_LEVELSET card and its mesh is automatically generated by the solver. The calculation of wave actions on the free surface, which is not sufficiently accurate for the analysis here, is a subject of LSTC development at the time of this writing (Caldichoury, 2020). The ICFD wave-height data are output using tracers and floaters. The tracers and the height of the floaters are not visualizable in the GUI (i.e., a snapshot similar to Figure 18a is not available), and so numerical errors due to the discrepancy between the output data and those calculated by the ICFD solver cannot be identified. However, since maxima of the tracer and floater data listed in Table 6 are not identical, one or both of the two methods does/do not necessarily output the wave heights calculated by the solver: similar issues for the ALE results of Figure 18a are expected.

The high-frequency content in NM-1 (e.g., *Sa*=2 to 3 g in 20 to 50 Hz shown in Figure 10a) drives distorted shapes and chaotic fluid responses on the free surface, which is also one of the contributors to the significant differences between the numerical and measured $d_{w,E}$ listed in Table 6a. Figure 19 presents snapshots of a video recorded for NM-1, showing ***TE*** and its attached float (purple), at t=0, 0.7, and 1.5 seconds. As shown in Figure 19a, the float rests on the free surface at t=0. Per Figure 19b, at t=0.7 second (the first peak shown in Figures 16 and 17a), the free surface is higher than the original level seen in Figure 19a and its shape is distorted around the boundary of the float. Figure 19c presents the water and the float at the time of the maximum wave height: t=1.5 seconds. As seen in the figure, the water splashes, the wave is discontinuous, and a free surface cannot be defined. The discontinuous fluid domain cannot be simulated using the ALE and ICFD models: see the water at t=1.5 seconds shown in Figures 18a and b, respectively. The waves generated in the NM-1 test and the numerical predictions are qualitatively different, and so the measured and numerical wave heights are not comparable. The wave-height transducer, built with a Temposonic gauge and a float, is designed for stable and continuous wave shapes and providing vertical displacements of the free surface at a point (i.e., monitoring location). The surfaces shown in Figures 19b and c cannot be characterized by measurement at a single point. If distorted and chaotic waves (e.g., Figures 19b and c) are the focus of the experiment, optical equipment capable of monitoring a three-dimensional displacement field would be needed. (Mir et al. (2020a) reported a maximum difference of 9% in wave heights at ***TE*** between ALE and test results for motions similar to NM-1. The difference is much smaller than the 58% reported here because the shaking did not result in the discontinuities of waves (Figures 19b and c) and the discrepancy between the tracer data and those calculated by the ALE solver was significantly mitigated[5].)

---

[5] Mir et al. (2020a) presented fluid-structure responses for one-, two-, and three-directional motions termed ECE, which were generated using the records of the 1940 El Centro earthquake shown in Table 2, namely, spectral shapes of the *x*-component of ECE and NM-1 (ES-1) are essentially identical. Numerical results for ECE, calculated using an ALE model, were compared with test data, and the maximum difference in wave heights was 9%. There are two reasons why the difference (9%) for ECE is significantly smaller than that for NM-1 (58%) reported here. First, the amplitude of ECE (PGA=0.5g) is smaller than that of NM-1 (PGA=1g), and so the chaotic fluid response of Figure 19c did not occur. Second, Mir et al. (2020a) extracted ALE results for wave heights using the tracer that was both closest to the monitoring location and on the free surface. Using Figure 18a as an example, the wave height at x=711 mm (***TE***) is not obtained using the tracer noted with a green circle, which lies above the free surface and overestimates the wave height, but using the tracer noted with an orange circle, which floats on the free surface.

Distorted and/or chaotic waves are observed neither in the tests nor in the numerical simulations for NM-2 and NM-3, for which the spectral accelerations at high frequencies are relatively small, as presented in Figures 10b and c. Wave heights are properly measured by the Temposonic gauges for the two motions, and so differences between the numerical results and the test data are associated with the numerical solutions. Per Tables 6b and c, the numerical and test results of wave-height amplitudes for NM-2 and NM-3 are in better agreement ($\leq \pm 12\%$) than those for NM-1. However, these amplitudes occur at different crests and troughs in the time series. For example, the maxima $d_{w,w}$ of the ALE and test results for NM-2 presented in Figure 16e are at 4.9 and 4.3 seconds, respectively. For NM-2 and NM-3, the differences between the ALE and test data at the time of maximum measured wave height (green lines in Figure 16) range between -14% and 5%. Companion results for the ICFD model (green lines in Figure 17) range between -6% and -41%, output using the tracers, and between -8% and -45%, output using the floaters. These data from both models and all output methods may not be sufficiently accurate for some nuclear, safety-related applications.

6. Recommendations, summary, and conclusions

Seismic fluid-structure-interaction (FSI) analysis of nuclear, safety-related, liquid-filled reactor vessels (tanks) will require verified and validated numerical models for seismic design, qualification, and risk assessment. This paper demonstrates a process of validation for seismic FSI models of tanks.

6.1. Recommendations for validation

To validate a numerical model for seismic FSI analysis, predictions of fluid-structure responses should be compared with test data. Three-directional seismic motions with a range of intensities should be used for the analysis to maximize the utility of the validation exercise. If the site of the reactor is known, motions consistent with the design-basis seismic hazard at the site could be used. Test results can be generated by performing experiments or extracted from available databases. If the difference between the numerical and test results at the peak of a given response is less than a required threshold (e.g., $\pm 10\%$), the model should be considered to be validated for calculating the response.

After validation[6], the numerical model could be modified for the boundary conditions, geometries, dimensions, and mechanical properties of the reactor. This model could then be used for calculating fluid-structure responses to three-directional seismic inputs. Although the validation provides high confidence in the capability of the numerical solver used and the modeling approach, a sensitivity analysis is required to optimize the mesh and the analysis time step (if an implicit solver is used) for the model of the reactor

[6] The numerical models would have to be verified before they are validated.

and the contained fluid. The mesh and time step should be capable of producing responses in the frequency range of interest.

6.2. Summary and conclusions

This study validates previously-verified numerical models using data generated from earthquake-simulator tests on a base-supported cylindrical tank filled with water. An ALE model and an ICFD model is developed based on the geometries, dimensions, mechanical properties, and boundary conditions of the test tank. Three sets of seismic inputs are used in the analysis, including one-, two-, or three-directional motions, and rocking motions that are associated with horizontal inputs and the flexibility of the tank support. The intensity of the motions is relatively strong, with PGAs ranging between 0.1 g and 1 g. For the models and the inputs used here, the run time of the ALE analysis is shorter than the ICFD analysis by a factor of 7.

Measured and numerically predicted hydrodynamic pressures on the tank wall, reactions at the tank base, and wave heights are compared. Different methods for outputting wave heights are described. Both ALE and ICFD models are validated for calculating reactions and hydrodynamic pressures away from the free surface (e.g., below the mid-height of the tank). Neither model is validated herein for calculating wave heights. For intense input motions with significant high-frequency content, the fluid response on the free surface can be chaotic, and wave heights can neither be measured nor can the shape of the free surface be characterized or predicted. For relatively stable waves that are measured correctly, the numerical predictions of wave height may not be sufficiently accurate. Accordingly, the use of the ALE and ICFD solvers is limited to FSI simulations with limited or no wave action (e.g., full tank). Further code development on simulating waves and outputting wave height data is needed. If wave height is small or not important, the ALE solver is recommended by the authors for seismic FSI analysis of tanks because it generates results similar to the ICFD solver (based on the presented data here) with a shorter run time.

7. Acknowledgments

The work presented herein was funded in part by the Advanced Research Projects Agency-Energy (ARPA-E), U.S. Department of Energy, under Award Number DE-AR0000978. The views and opinions of the authors expressed herein do not necessarily state or reflect those of the U.S. Government or any agency thereof.

8. References

ANSYS Inc. (2005). "ANSYS 10.0 user's manual." Cecil Township, PA.

Bandyopadhyay, K., Cornell, C. A., Costantino, C., Kennedy, R., Miller, C., and Veletsos, A. S. (1995). "Seismic design and evaluation guidelines for the Department of Energy high-level waste storage tanks and appurtenances." *BNL 52361(REV. 10/95)/UC-406/UC-510*, Brookhaven National Laboratory, Associated Universities, Inc., Upton, NY.

Caldichoury, I. (2019, 8 Jul). Personal communication, LSTC Technical Support <support@lstc.com>.

Caldichoury, I. (2020, 3 Jan). Personal communication, LSTC Technical Support <support@lstc.com>.

Calugaru, V., and Mahin, S. A. (2009). "Experimental and analytical studies of fixed base and seismically isolated liquid storage tanks." *Tran., Proceedings, International Conference on Advances in Experimental Structural Engineering*, , San Francisco, CA.

Chalhoub, M. S., and Kelly, J. M. (1988). "Theoretical and experimental studies of cylindrical water tanks in base isolated structures." *UCB/EERC-88/07*, Earthquake Engineering Research Center, University of California at Berkeley, Berkeley, CA.

Chen, S., and Rosenberg, G. (1975). "Dynamics of a coupled shell-fluid system." *Nuclear Engineering and Design*, 32(3), 302-310.

Chen, S., Wambsganss, M., and Jendrzejczyk, J. (1976). "Added mass and damping of a vibrating rod in confined viscous fluids." *Journal of Applied Mechanics*, 43(2), 325-329.

Chung, H., and Chen, S. (1976). "Vibration of a group of circular cylinders in a confined fluid." *ANL-CT-76-25*, Argonne National Laboratory (ANL), Lemont, IL.

Chung, H., and Chen, S. (1977). "Vibration of a group of circular cylinders in a confined fluid." *Journal of Applied Mechanics*, 44(2), 213-217.

Compagnoni, M. E., and Curadelli, O. (2018). "Experimental and numerical study of the response of cylindrical steel tanks under seismic excitation." *International Journal of Civil Engineering*, 16(7), 793-805.

Dassault Systèmes (2018). "ABAQUS 2018-unified FEA products." Vélizy-Villacoublay, France.

Do, I. (2019, 3 Apr). Personal communication, LSTC Technical Support <support@lstc.com>.

Dong, R. G. (1978). "Effective mass and damping of submerged structures." *UCRL-52342*, Lawrence Livermore Laboratory, Livermore, CA.

European Committee for Standardization (CEN) (1998). "Soils, tanks and pipelines." *Eurocode 8: design provision of earthquake resistance of structures*, Brussels, Belgium.

Fujita, K., Ito, T., Shimomura, T., and Morishita, M. (1984). "Aseismic study on the reactor vessel of a fast breeder reactor." *Nuclear Engineering and Design*, 83(1), 47-61.

Gluekler, E. L. (1997). "U.S. advanced liquid metal reactor (ALMR)." *Progress in Nuclear Energy*, 31(1-2), 43-61.

Goudarzi, M. A., and Sabbagh-Yazdi, S. R. (2012). "Investigation of nonlinear sloshing effects in seismically excited tanks." *Soil Dynamics and Earthquake Engineering*, 43, 355-365.

Haroun, M. A. (1983). "Vibration studies and tests of liquid storage tanks." *Earthquake Engineering and Structural Dynamics*, 11(2), 179-206.

Hoskins, L. M., and Jacobsen, L. S. (1934). "Water pressure in a tank caused by a simulated earthquake." *Bulletin of the Seismological Society of America*, 24(1), 1-32.

Huang, Y., Sturt, R., and Willford, M. (2019). "A damping model for nonlinear dynamic analysis providing uniform damping over a frequency range." *Computers and Structures*, 212, 101-109.

Huang, Y. (2020, Jul 27). Personal communication, Ansys, Inc., Email.

Jacobsen, L. S. (1949). "Impulsive hydrodynamics of fluid inside a cylindrical tank and of fluid surrounding a cylindrical pier." *Bulletin of the Seismological Society of America*, 39(3), 189-204.

Livermore Software Technology Corporation (LSTC) (2018a). "LS-DYNA keyword user's manual-R11." LSTC, Livermore, CA.

Livermore Software Technology Corporation (LSTC) (2018b). "LS-DYNA SMP_d_Dev_126632." Livermore, CA.

Livermore Software Technology Corporation (LSTC) (2018c). "LS-PrePost V4.7." Livermore, CA.

Livermore Software Technology Corporation (LSTC) (2019). "LS-DYNA SMP_d_R11.1.0." Livermore, CA.

Malhotra, P. K., Wenk, T., and Wieland, M. (2000). "Simple procedure for seismic analysis of liquid-storage tanks." *Structural Engineering International*, 10(3), 197-201.

Mazzoni, S., McKenna, F., Scott, M. H., and Fenves, G. L. (2009). "Open system for earthquake engineering simulation user manual, version 2.0." Pacific Earthquake Engineering Research Center (PEER), University of California, Berkeley, CA.

Mir, F. U. H., Yu, C.-C., Cohen, M., Bardet, P., Coleman, J. L., and Whittaker, A. S. (2019). "Dataset generation for validation of fluid-structure interaction models." *Tran., 25th International Conference on Structural Mechanics in Reactor Technology (SMiRT-25)*, Charlotte, NC.

Mir, F. U. H., Yu, C.-C., and Whittaker, A. S. (2020a). "Experimental and numerical studies of seismic fluid structure interaction in a base-supported cylindrical vessel." *Earthquake Engineering and Structural Dynamics*, 1-19.

Mir, F. U. H., Yu, C.-C., and Whittaker, A. S. (2020b). "Experiments for validation of FSI models for seismic response of advanced reactor internals." *Proc., 17th World Conference on Earthquake Engineering (17WCEE)*, Sendai, Japan.

Mir, F. U. H., Yu, C.-C., Charkas, H., and Whittaker, A. S. (2020c). "Validation of numerical models for seismic fluid-structure interaction analysis of advanced reactors." *Proc., International Congress on Advances in Nuclear Power Plants (ICAPP 2020)*, Abu Dhabi, United Arab Emirates.

Mir, F. U. H., Yu, C.-C., and Whittaker, A. S. (2021). "Rocking response of liquid-filled cylindrical tanks." *Earthquake Spectra*, 1-12.

Morris, B. T. (1938). "A laboratory model study of the behavior of liquid-filled tanks in earthquakes." Dissertation, presented to Standford University, in partial fulfillment of the requirements for the degree of Doctor of Philosophy.

Myrillas, K., Planquart, P., Simonini, A., Buchlin, J.-M., and Schyns, M. (2017). "CFD and experimental investigation of sloshing parameters for the safety assessment of HLM reactors." *Nuclear Engineering and Design*, 312, 317-326.

OpenCFD Ltd. (2020). "OpenCFD Release OpenFOAM® v2012 (20 12)." <https://www.openfoam.com/releases/openfoam-v2012/>. (Feb 22, 2021).

Pacific Earthquake Engineering Research (PEER) "PEER ground motion database." <http://peer.berkeley.edu/peer_ground_motion_database>. (Jan. 12, 2019).

Pal, N., Bhattacharyya, S., and Sinha, P. (2001). "Experimental investigation of slosh dynamics of liquid-filled containers." *Experimental Mechanics*, 41(1), 63-69.

Papazafeiropoulos, G., and Plevris, V. (2018). "OpenSeismoMatlab: a new open-source software for strong ground motion data processing." *Heliyon*, 4(9), e00784.

Park, J.-B., Choi, Y., Lee, S.-J., Park, N.-C., Park, K.-S., Park, Y.-P., and Park, C.-I. (2014). "Modal characteristic analysis of the APR1400 nuclear reactor internals for seismic analysis." *Nuclear Engineering and Technology*, 46(5), 689-698.

Radnić, J., Grgić, N., Kusić, M. S., and Harapin, A. (2018). "Shake table testing of an open rectangular water tank with water sloshing." *Journal of Fluids and Structures*, 81, 97-115.

Sangsari, M. K., and Hosseinzadeh, N. (2014). "Shake table study of impulsive and convective damping coefficients for steel cylindrical tanks and comparison with API 650." *Journal of Seismology and Earthquake Engineering*, 16(2), 129.

Thomas, T. H., Yasui, G., Graham, R. H., Williamson, R. A., Lowe, R. E., and Hoak, W. (1963). "Nuclear reactors and earthquakes." ***TID-7024***, Division of Reactor Development, United States Atomic Energy Commission, Washington DC.

Veletsos, A. (1984). "Seismic response and design of liquid storage tanks." ***Guidelines for the seismic design of oil and gas pipeline systems***, Committee on Gas and Liquid Fuel Lifelines, American Society of Civil Engineers (ASCE), Reston, VA, 255-370.

Veletsos, A., and Tang, Y. (1986). "Dynamics of vertically excited liquid storage tanks." ***Journal of Structural Engineering***, 112(6), 1228-1246.

Veletsos, A., and Tang, Y. (1987). "Rocking response of liquid storage tanks." ***Journal of Engineering Mechanics***, 113(11), 1774-1792.

Yu, C.-C., and Whittaker, A. S. (2020a). "Analytical solutions for seismic fluid-structure interaction of head-supported cylindrical tanks." ***Journal of Engineering Mechanics***, 146(10), 04020112.

Yu, C.-C., and Whittaker, A. S. (2020b). "Review of analytical studies on seismic fluid-structure interaction of base-supported cylindrical tanks." ***in press, Engineering Structures***.

Yu, C.-C., and Whittaker, A. S. (2020c). "Analytical and numerical studies of seismic fluid-structure interaction in liquid-filled vessels." ***MCEER-20-0003***, University at Buffalo, Buffalo, NY.

Yu, C.-C., and Whittaker, A. S. (2021). "Verification of numerical models for seismic fluid-structure-interaction analysis of internal components in liquid-filled advanced reactors." ***Earthquake Engineering and Structural Dynamics***, 1-21.

Zhu, M., McKenna, F., and Scott, M. H. (2018). "OpenSeesPy: Python library for the OpenSees finite element framework." ***SoftwareX***, 7, 6-11.

FIGURES

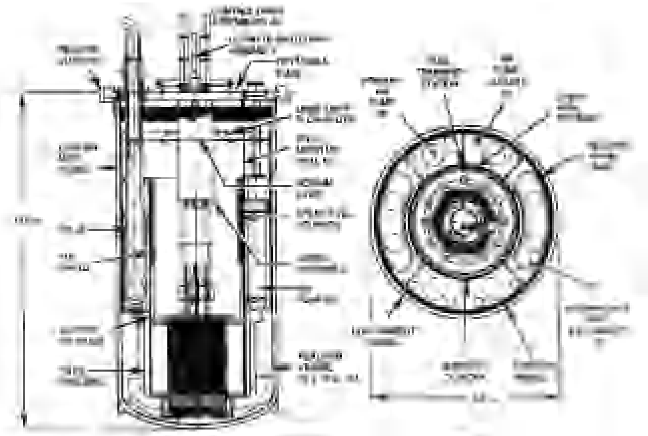

Figure 1. Prototype sodium fast reactor, including a reactor vessel, internal components, and a liquid sodium coolant (Gluekler, 1997)

(a) (b)

Figure 2. Earthquake-simulator tests: (a) base-supported steel tank filled with water (dyed green), $R = 0.76$ m, $H_s = 2$ m, $h = 7.92$ mm, and $H = 1.6$ m, view from the south and top; (b) earthquake simulator, coordinates (x, y, z), cardinal directions (N, S, E, W)

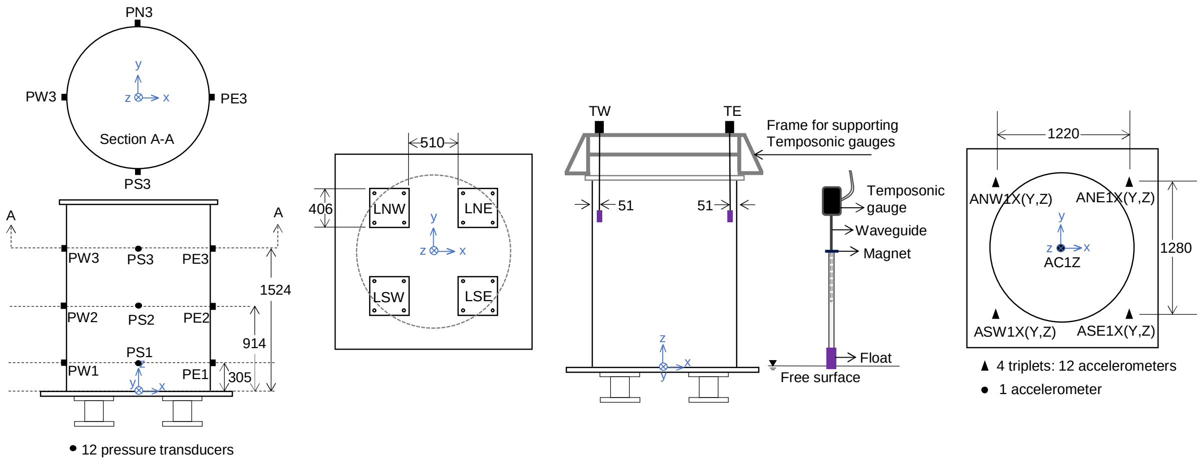

(a) (b) (c) (d)

Figure 3. Instrumentation, unit: mm: (a) pressure transducers; (b) load cells; (c) Temposonic gauges for wave measurement; (d) accelerometers on the base plate

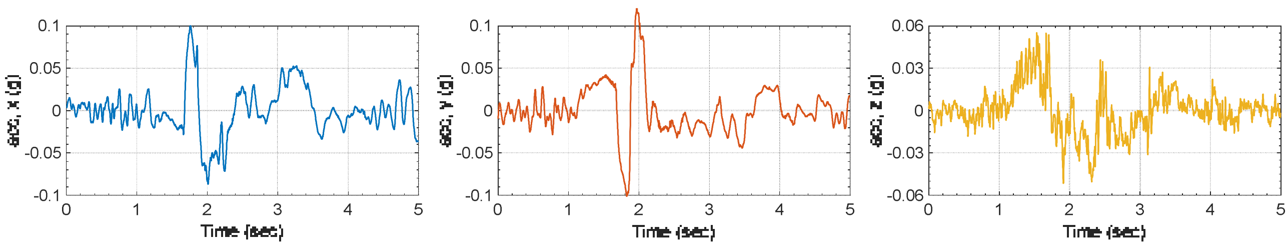

(a) (b) (c)

Figure 4. Time series of earthquake-simulator input ES-3, PGAs and time scaled per Table 2: (a) *x* component; (b) *y* component; (c) *z* component

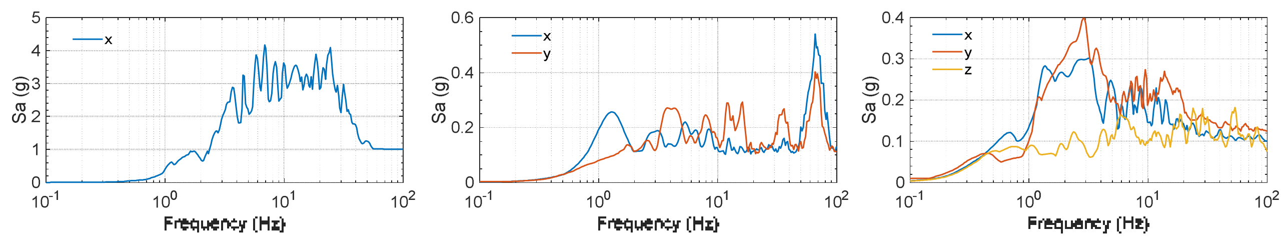

(a) (b) (c)

Figure 5. Acceleration response spectra of the earthquake-simulator (ES) inputs presented in Table 2, damping ratio of 2%: (a) ES-1; (b) ES-2; (c) ES-3

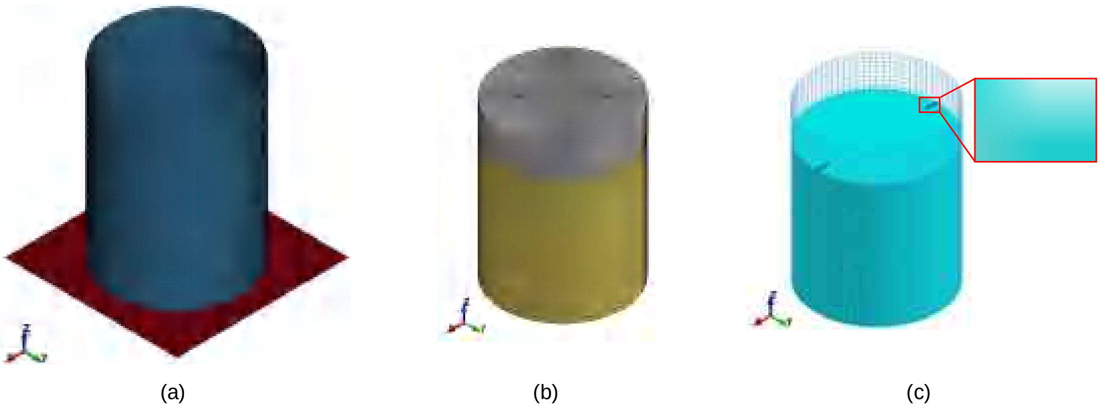

Figure 6. ALE model of the test tank with $R = 0.76$ m, $H_s = 2$ m, $h = 7.92$ mm, and $H = 1.6$ m: (a) tank wall and base plate; (b) water and vacuum; (c) water in the tank, tracers, t=0

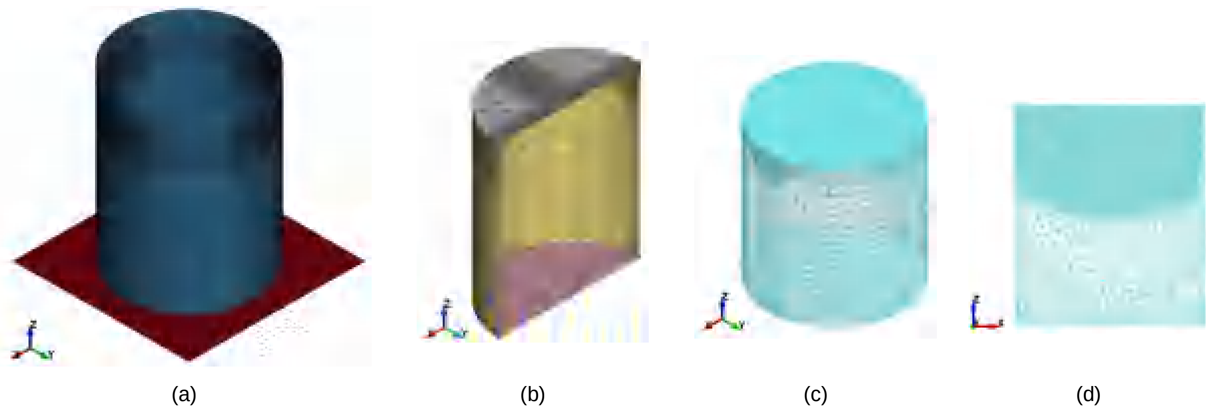

Figure 7. ICFD model of the test tank with $R = 0.76$ m, $H_s = 2$ m, $h = 7.92$ mm, and $H = 1.6$ m: (a) tank wall and base plate; (b) surfaces for a half fluid domain; (c) water, t=0; (d) fluid domain, *x-z* cross section, t=0

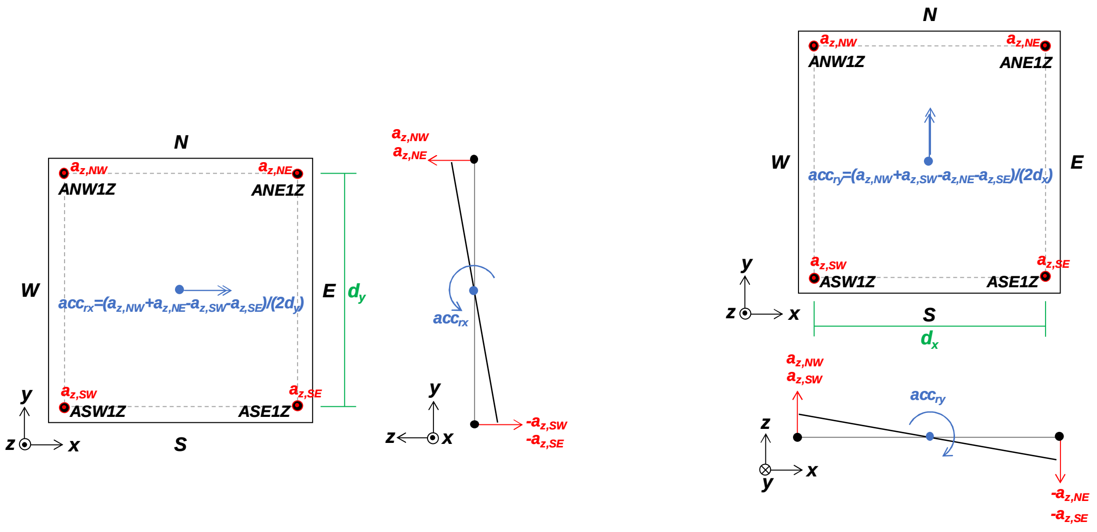

(a) (b)

Figure 8. Rocking motions at the center of the rigid base plate used in the numerical models, calculated using vertical accelerations measured around the four corners: (a) *rx* component, acc_{rx} ; (b) *ry* component, acc_{ry}

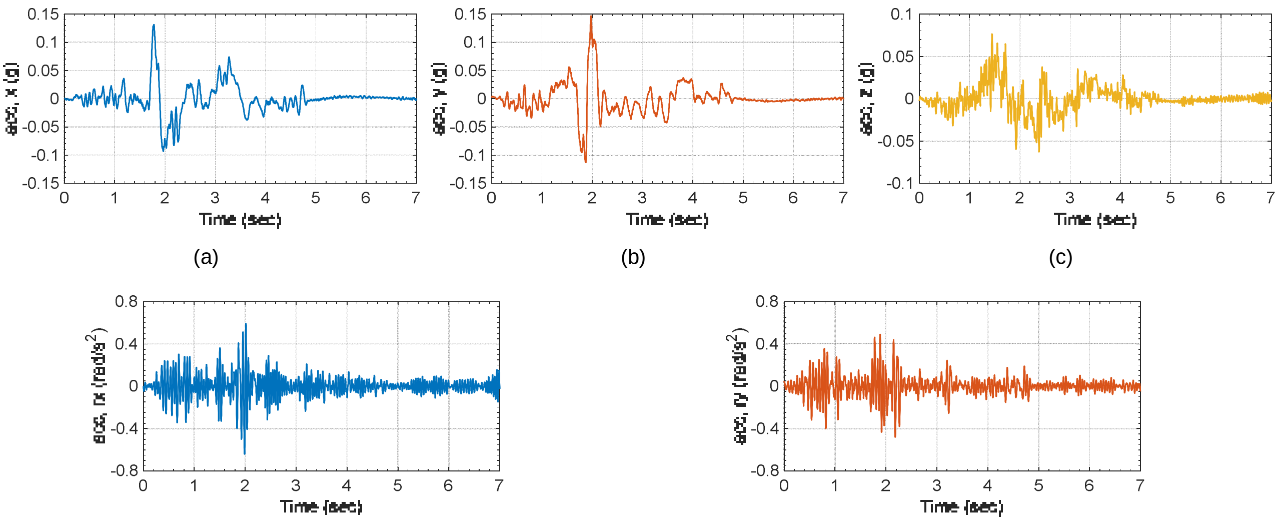

(a) (b) (c)

(d) (e)

Figure 9. Time series for numerical-model input NM-3, derived using filtered and baseline corrected accelerations of the base plate for ES-3: (a) *x* component; (b) *y* component; (c) *z* component; (d) *rx* component; (e) *ry* component

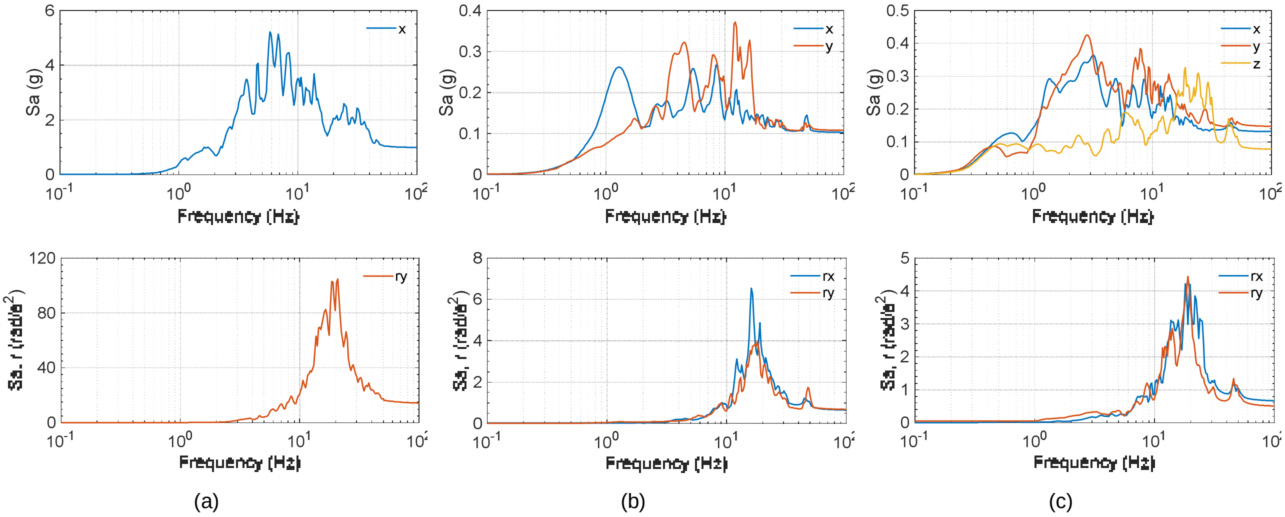

Figure 10. Acceleration response spectra of the numerical-model (NM) inputs, *x*, *y*, *z*, *rx*, and *ry* components, damping ratio of 2%: (a) NM-1; (b) NM-2; (c) NM-3

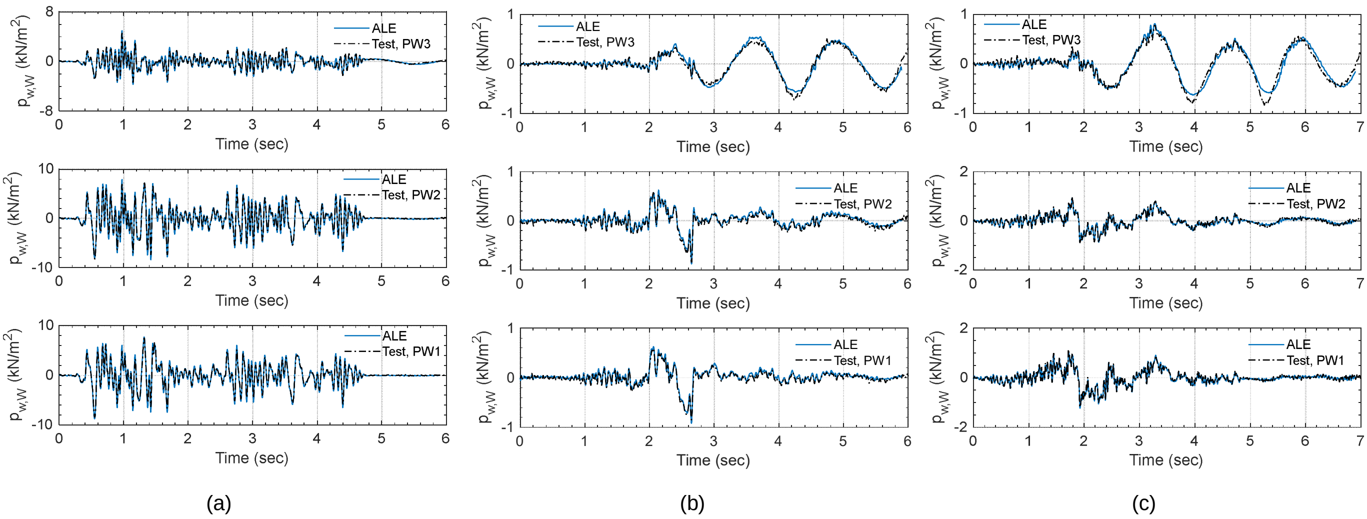

Figure 11. Time series of hydrodynamic pressures on the west face of the tank wall $p_{w,W}$, ALE model and earthquake-simulator tests: (a) NM-1; (b) NM-2; (c) NM-3

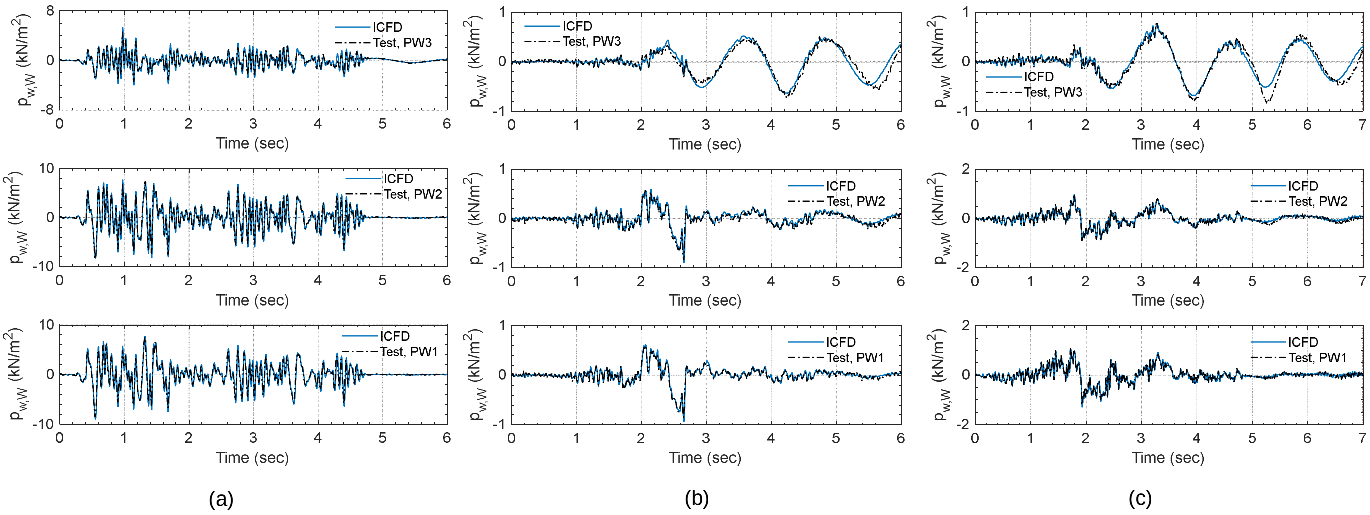

Figure 12. Time series of hydrodynamic pressures on the west face of the tank wall $p_{w,W}$, ICFD model and earthquake-simulator tests: (a) NM-1; (b) NM-2; (c) NM-3

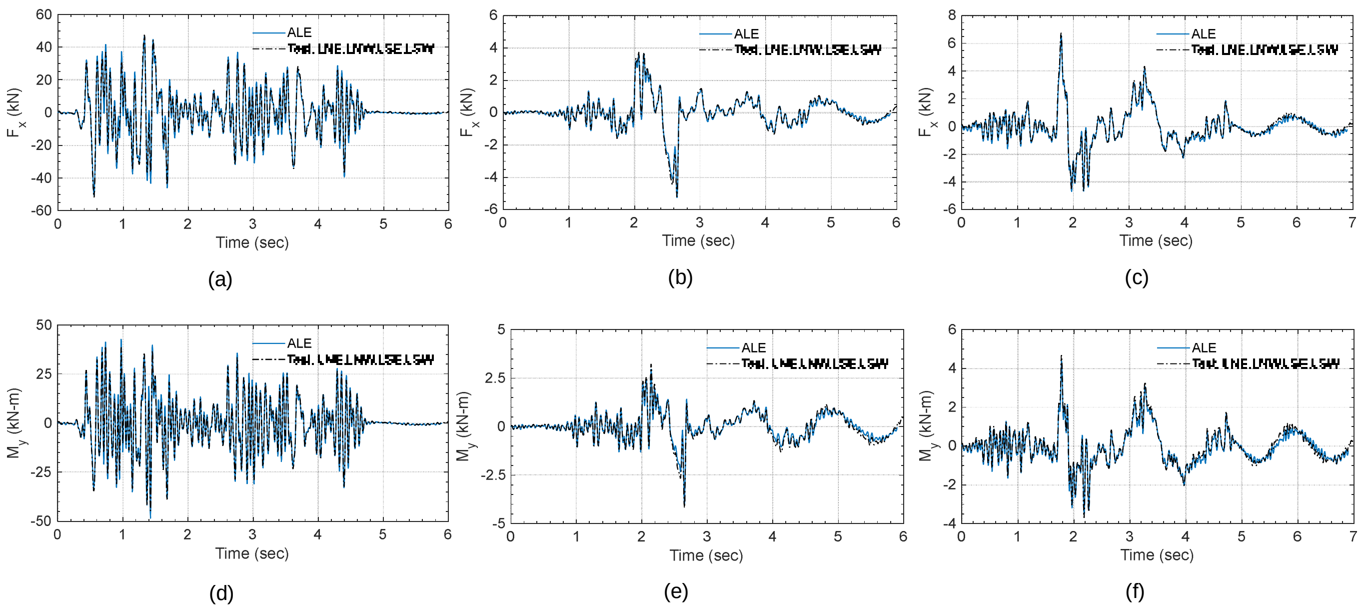

Figure 13. Time series of reactions at the tank base, ALE model and earthquake-simulator tests: (a) F_x for NM-1; (b) F_x for NM-2; (c) F_x for NM-3; (d) M_y for NM-1; (e) M_y for NM-2; (f) M_y for NM-3

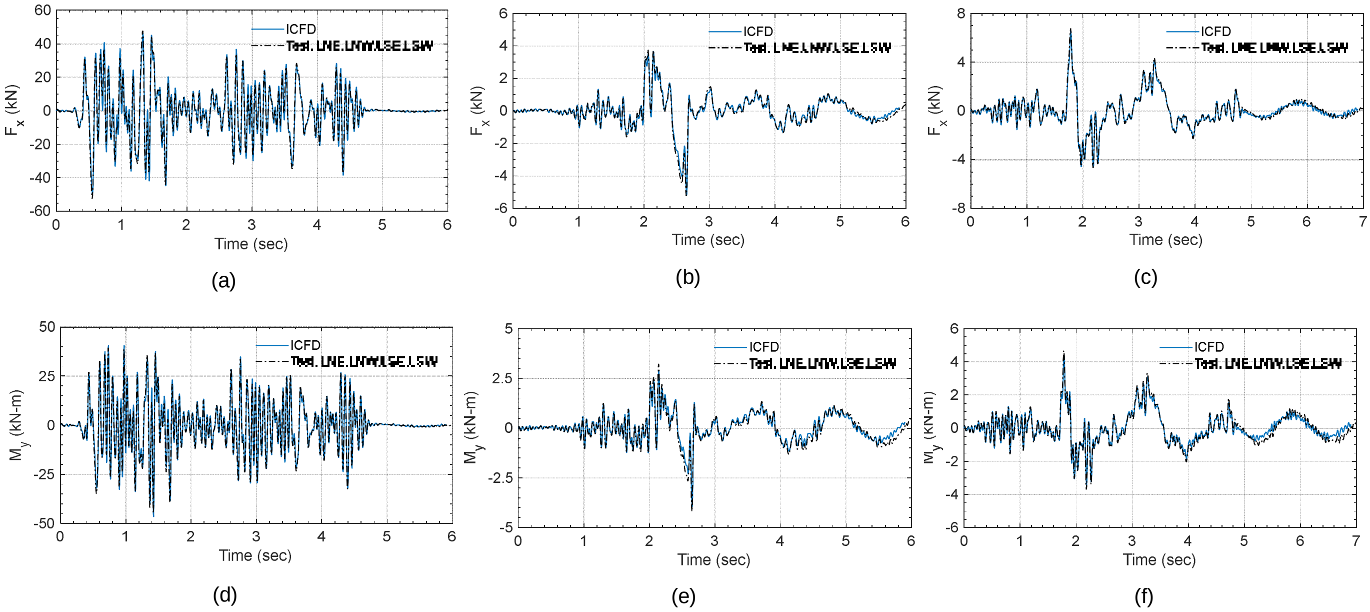

Figure 14. Time series of reactions at the tank base, ICFD model and earthquake-simulator tests: (a) F_x for NM-1; (b) F_x for NM-2; (c) F_x for NM-3; (d) M_y for NM-1; (e) M_y for NM-2; (f) M_y for NM-3

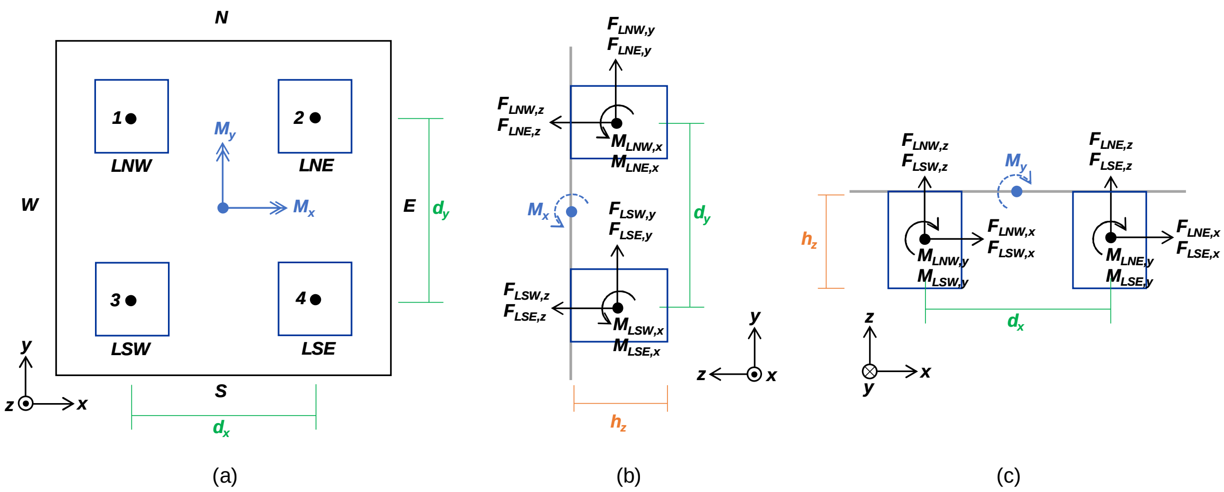

Figure 15. Reaction moments, M_x and M_y, at the center of the base plate derived using forces and moments measured by the four load cells, *LNE*, *LNW*, *LSE* and *LSW*: (a) plan view; (b) *N-S* section; (c) *E-W* section

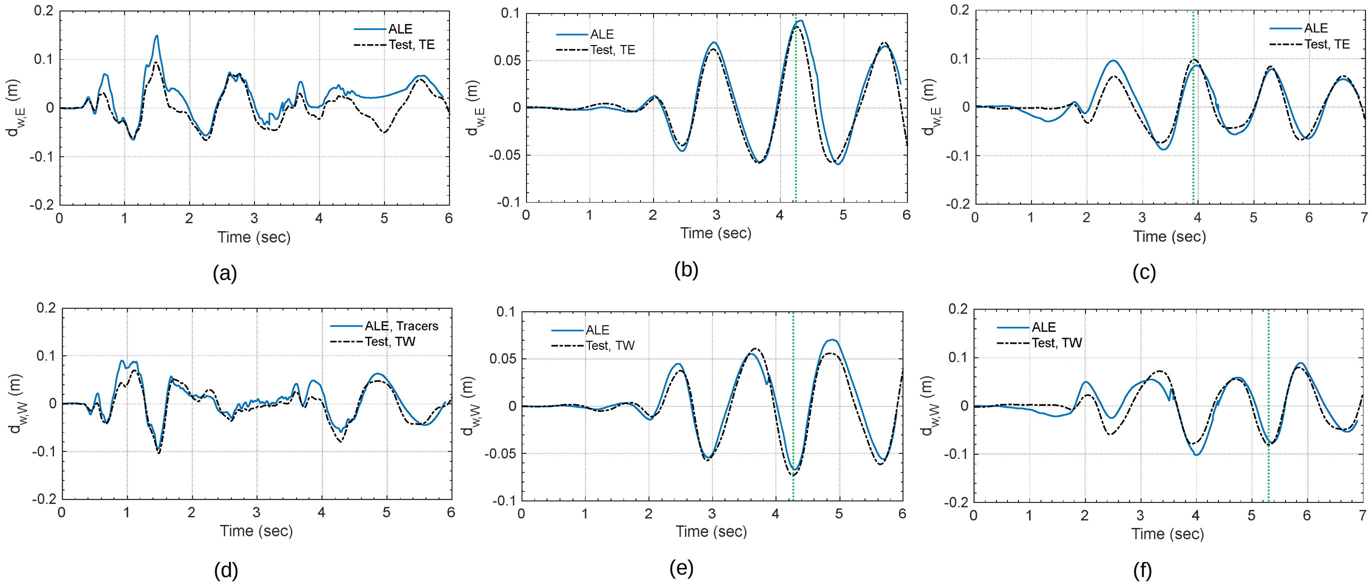

Figure 16. Time series of wave heights, ALE model and earthquake-simulator tests: (a) $d_{w,E}$ for NM-1; (b) $d_{w,E}$ for NM-2; (c) $d_{w,E}$ for NM-3; (d) $d_{w,W}$ for NM-1; (e) $d_{w,W}$ for NM-2; (f) $d_{w,W}$ for NM-3

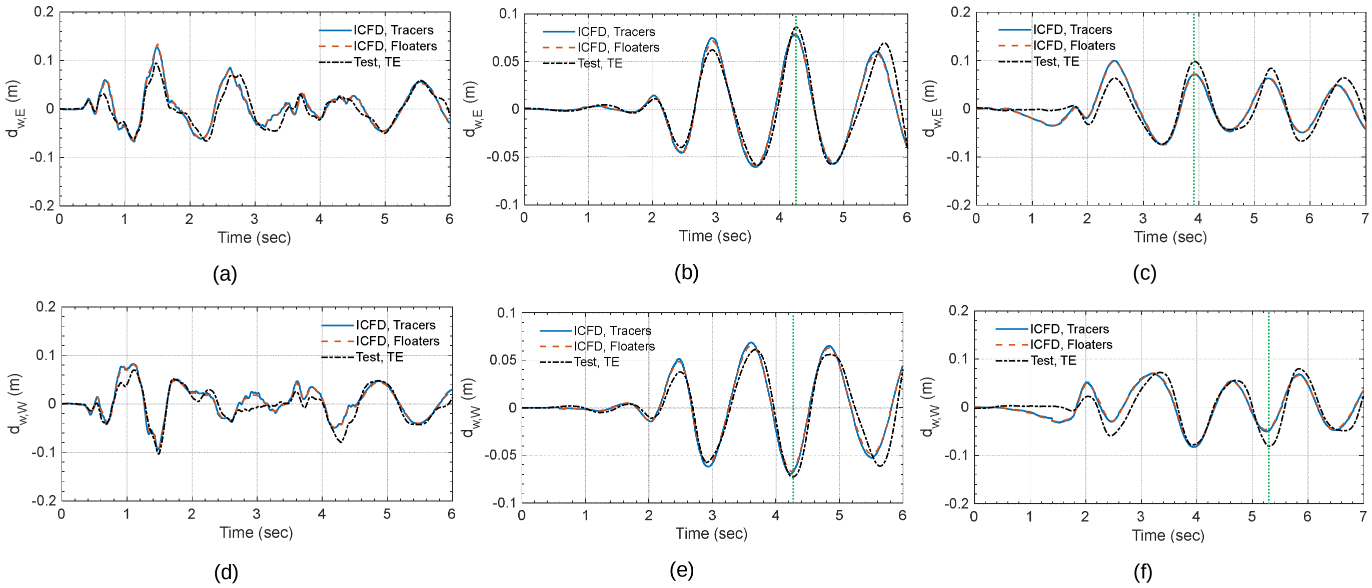

Figure 17. Time series of wave heights, ICFD model and earthquake-simulator tests, two output methods: (a) $d_{w,E}$ for NM-1; (b) $d_{w,E}$ for NM-2; (c) $d_{w,E}$ for NM-3; (d) $d_{w,W}$ for NM-1; (e) $d_{w,W}$ for NM-2; (f) $d_{w,W}$ for NM-3

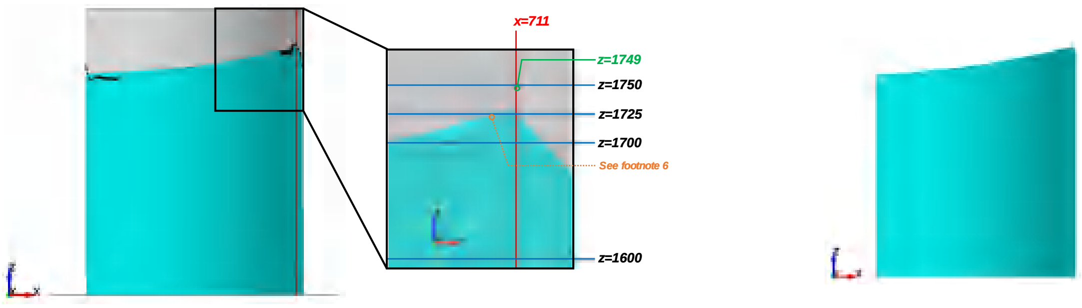

(a) (b)

Figure 18. Water in the numerical models for NM-1 at t=1.5 seconds: (a) ALE model, magnified around *TE*, unit: mm; (b) ICFD model

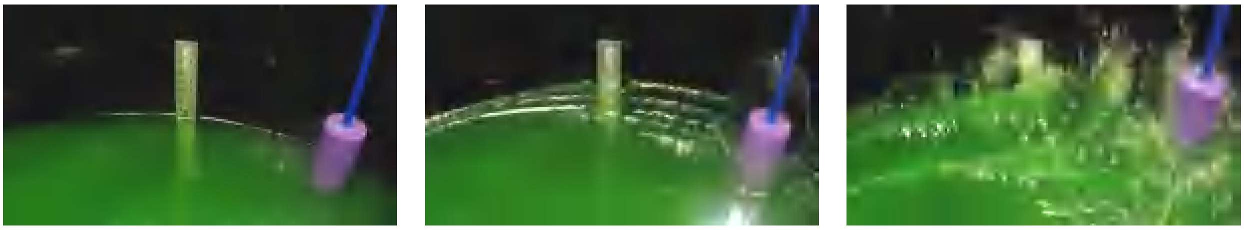

(a) (b) (c)

Figure 19. Snapshots of a video recorded for NM-1 (ES-1) showing the Temposonic gauge *TW*, its attached float (purple), and surrounding water: (a) t=0; (b) t=0.7 second; (c) t=1.5 seconds

TABLES

Table 1. Computer codes used for calculating nonlinear and linear fluid responses, fluid-mechanics solvers, and fluid elements and materials for structural mechanics solvers

Computer code	Fluid-mechanics solver: nonlinear fluid response	Fluid element and material: linear fluid response
ANSYS	Fluent and CFX	FLUID29, FLUID30, FLUID 38, FLUID80, FLUID129, FLUID130, FLUID220, and FLUID221
ABAQUS	Computational Fluid Dynamics (CFD) and Coupled Eulerian and Lagrangian (CEL)	AC3D10, AC3D4, AC3D20, AC3D8R
LS-DYNA	Arbitrary Lagrangian-Eulerian (ALE), Incompressible Computational Fluid Dynamics (ICFD), and Smoothed Particle Hydrodynamics (SPH)	MAT_ELASTIC_FLUID, MAT_ACOUSTIC, and MAT_NULL
OpenFOAM	Computational Fluid Dynamics (CFD)	--
OpenSees	Particle finite element method (PFEM) in OpenSeesPy (Zhu et al., 2018)	--

Table 2. Input motion time series[a] used for earthquake-simulator tests

	Event	Year	Station	Direction[b]	Original PGA (g)	Scaled PGA (g)	Time scale[c]
ES-1	El Centro earthquake (Imperial Valley-02)	1940	El Centro Array #9	180 (x)	0.28	1.0	$1/\sqrt{10}$
ES-2	Hualien earthquake	2018	HWA019	EW (x)	0.39	0.1	$1/\sqrt{10}$
				NS (y)	0.37	0.09	
ES-3	Chi-Chi earthquake	1999	TCU052	EW (x)	0.36	0.1	$1/\sqrt{10}$
				NS (y)	0.45	0.13	
				Up (z)	0.19	0.06	

a. Ground motion records of the El Centro and Chi-Chi earthquakes are extracted from the PEER Ground Motion Database (http://ngawest2.berkeley.edu/, accessed on March 18, 2019), and those of the Hualien earthquake are provided by the National Center for Research on Earthquake Engineering (NCREE), Taiwan (https://www.ncree.narl.org.tw/)

b. Directions are described in the dataset of the ground motion records, and x, y, and z in the parentheses represent the input directions of the earthquake simulator (see Figure 2b)

c. Time scale compressed by a factor of $\sqrt{10}$ per the ratio of the heights of the test tank (H_s = 2 m) and the reactor vessel of Figure 1 (H_s = 19.6 m): a length scale of approximately 1/10

Table 3. Mechanical properties assigned to the elements of the tank, water, and vacuum, ALE and ICFD models

		ALE	ICFD
Tank wall and base	Density, ρ_s	7880 kg/m^3	
	Elastic modulus, E_s	2×1011 N/m^2	
	Poisson's ratio, υ_s	0.27	
Water	Density, ρ_w	1000 kg/m^3	
	Viscosity, μ_w	10^{-3} N/m^2-s	
	Bulk modulus, K_w	2.15×10^9 N/m^2	--[a]
Vacuum	Density, ρ_v	--[b]	0
	Viscosity, μ_v		0

a. The ICFD solver analyzes only incompressible fluids, and so K_w is not used in the model.
b. The vacuum in the ALE model is assigned void properties through the *INITIAL_VOID card

Table 4. Masses of the tank wall, base plate, and water, ALE and ICFD models

Component	Mass (kg)
Tank wall	593
Base plate	1418
Water	2918
Total	4929

Table 5. Input motions used for the numerical models at the center of the base plate and their associated earthquake-simulator (ES) inputs used in the experiments

Numerical-model input	Directions[a]	Earthquake-simulator input[b]
NM-1	*x*, *ry*	ES-1: *x*
NM-2	*x*, *y*, *rx*, *ry*	ES-2: *x*, *y*
NM-3	*x*, *y*, *z*, *rx*, *ry*	ES-3: *x*, *y*, *z*

a. Directions based on the coordinates used for the numerical models (Figures 6 and 7) and the earthquake simulator (Figure 2b)
b. More information presented in Table 2

Table 6. Maximum absolute FSI responses of the test tank, extracted from time series of test, ALE, and ICFD results

(a) input motion: NM-1 for numerical analysis and ES-1 for earthquake simulator

Response	Test		ALE	ICFD
	Instrument	Measured response	Calculated response (difference[a])	Calculated response (difference[a])
$p_{w,E}$ (kN/m^2)	*PE3* *PE2* *PE1*	6.0 9.2 9.9	6.5 (9%) 9.8 (6%) 10.2 (3%)	7.0 **(17%)** 9.8 (6%) 10.2 (3%)
$p_{w,W}$ (kN/m^2)	*PW3* *PW2* *PW1*	4.6 8.3 8.4	5.0 (9%) 8.4 (2%) 8.8 (4%)	5.4 **(18%)** 8.2 (-1%) 8.9 (6%)
F_x (kN)	*LNE, LNW, LSE, LSW*	51.9	50.4 (-3%)	49.4 (-5%)
M_y (kN-m)		44.7	48.5 (9%)	46.7 (4%)
$d_{w,E}$ (m)	*TE*	94	149 **(58%)**	127 **(34%)**[b] 134 **(42%)**[c]
$d_{w,W}$ (m)	*TW*	103	94 (-9%)	94 (-9%)[b] 88 **(-15%)**[c]

(b) input motion: NM-2 for numerical analysis and ES-2 for earthquake simulator

Response	Test		ALE	ICFD
	Instrument	Measured response	Calculated response (difference[a])	Calculated response (difference[a])
$p_{w,E}$ (kN/m^2)	*PE3* *PE2* *PE1*	0.56 0.81 0.80	0.53 (-6%) 0.86 (6%) 0.87 (9%)	0.58 (3%) 0.88 (8%) 0.86 (8%)
$p_{w,W}$ (kN/m^2)	*PW3* *PW2* *PW1*	0.74 0.84 0.85	0.57 **(-23%)** 0.88 (4%) 0.92 (8%)	0.63 **(-14%)** 0.90 (6%) 0.94 (10%)
$p_{w,N}$ (kN/m^2)	*PN3* *PN2* *PN1*	0.39 0.81 0.92	0.39 (-1%) 0.82 (1%) 0.91 (-2%)	0.36 (-8%) 0.81 (0%) 0.90 (-2%)
$p_{w,S}$ (kN/m^2)	*PS3* *PS2* *PS1*	0.41 0.78 0.87	0.40 (-1%) 0.71 (-8%) 0.78 (-10%)	0.37 (-9%) 0.72 (-8%) 0.80 (-8%)
F_x (kN)	*LNE, LNW, LSE, LSW*	5.21	5.25 (1%)	5.19 (0%)
F_y (kN)		4.99	4.71 (-5%)	4.64 (-7%)
M_x (kN-m)		3.65	3.38 (-8%)	3.31 (-9%)
M_y (kN-m)		4.19	3.98 (-5%)	3.93 (-6%)
$d_{w,E}$ (mm)	*TE*	86	92 (8%)	79 (-9%)[b] 78 (-10%)[c]
$d_{w,W}$ (mm)	*TW*	73	71 (-3%)	70 (-4%)[b] 67 (-8%)[c]

Table 6. Maximum absolute FSI responses of the test tank, extracted from time series of test, ALE, and ICFD results (continued)

(c) input motion: NM-3 for numerical analysis and ES-3 for earthquake simulator

Response	Test		ALE	ICFD
	Instrument	Measured response	Calculated response (difference[a])	Calculated response (difference[a])
$p_{w,E}$ (kN/m^2)	*PE3*	0.76	0.75 (0%)	0.74 (-2%)
	PE2	1.18	1.17 (-1%)	1.18 (0%)
	PE1	1.44	1.39 (-3%)	1.39 (-3%)
$p_{w,W}$ (kN/m^2)	*PW3*	0.83	0.81 (-3%)	0.77 (-8%)
	PW2	0.99	0.92 (-6%)	0.98 (-1%)
	PW1	1.19	1.23 (3%)	1.28 (8%)
$p_{w,N}$ (kN/m^2)	*PN3*	0.49	0.42 **(-14%)**	0.43 **(-12%)**
	PN2	1.36	1.31 (-4%)	1.34 (-1%)
	PN1	1.59	1.51 (-5%)	1.54 (-3%)
$p_{w,S}$ (kN/m^2)	*PS3*	0.47	0.47 (-2%)	0.49 (3%)
	PS2	1.06	1.00 (-6%)	1.03 (-3%)
	PS1	1.28	1.18 (-8%)	1.22 (-5%)
F_x (kN)	*LNE, LNW, LSE, LSW*	6.76	6.58 (-3%)	6.54 (-3%)
F_y (kN)		7.31	7.08 (-3%)	6.97 (-5%)
F_z (kN)		3.90	3.77 (-3%)	3.72 (-4%)
M_x (kN-m)		5.38	4.90 (-9%)	4.83 (-10%)
M_y (kN-m)		4.68	4.39 (-6%)	4.35 (-7%)
$d_{w,E}$ (m)	*TE*	98	94 (-4%)	100 (2%)[b] 100 (2%)[c]
$d_{w,W}$ (m)	*TW*	81	91 **(12%)**	83 (3%)[b] 80 (-1%)[c]

a. Percentage difference of FSI responses calculated using the numerical models with respect to test results, to the nearest 1%; differences greater than 10% bolded

b. Calculated using data of tracers

c. Calculated using data of floaters